ISSN 0023-1584, Kinetics and Catalysis, 2010, Vol. 51, No. 3, pp. 327–336. © Pleiades Publishing, Ltd., 2010.
Original Russian Text © A.A. Chernov, O.P. Korobeinichev, C. Modenese, L.G. Krishtopa, L.N. Krasnoperov, 2010, published in Kinetika i Kataliz, 2010, Vol. 51, No. 3, pp. 347–357.

Kinetics, Products, and Mechanism of Ethane Destruction in Corona Discharge: Experiments and Simulation

A. A. Chernov[a], O. P. Korobeinichev[a], C. Modenese[b], L. G. Krishtopa[b], and L. N. Krasnoperov[b]

[a] *Institute of Chemical Kinetics and Combustion, Siberian Branch, Russian Academy of Sciences, Novosibirsk, 630090 Russia*

[b] *New Jersey Institute of Technology, Newark, United States*

e-mail: chernov@kinetics.nsc.ru

Received February 10, 2009

Abstract—Ethane destruction in corona discharge was studied in a flow reactor. Samples from the reactor were analyzed by GC/MS and on a quadrupole mass spectrometer. Corona discharge was initiated at atmospheric pressure and room temperature in a cylindrical flow reactor with a dielectric barrier and an axial high-voltage electrode. The flow rate of the initial mixture was varied between 0.17 and 4.8 cm^3/s; the discharge power, between 0.01 and 8.0 W. The radiation yield was 0.5 molecule/100 eV for 1% ethane in air. Simulation was carried out using the kinetic mechanism consisting of 809 reactions involving 85 types of molecules, atoms, radicals, and excited species. The so-called free-radical mechanism that we developed led to an underestimated ethane destruction efficiency. The model qualitatively describes the product composition and the concentrations of its main components, but it provides no quantitative fit to experimental data, particularly for low initial ethane concentrations. New products hitherto unreported in the literature—methyl nitrate, ethyl nitrate, and acetic acid—were identified and quantified. The results are interpreted in terms of ionic reactions as a part of the destruction mechanism. These reactions are of particular significance in dilute mixtures and at low hydrocarbon concentrations in the initial mixture.

DOI: 10.1134/S0023158410030018

In the last decade, corona discharge has attracted considerable interest as the basic element of a promising technology for purification of air streams [1–19]. This technique proved to be applicable to a wide variety of contaminants and is discussed as a method of destruction of hydrocarbons (volatile organic compounds) [1–6], organophosphorus compounds [7–9], NO_x [10–14], SO_x [14–17], soot [18], and halohydrocarbons (freons) [19]. Recently, the corona discharge has gained new interest in the context of the nonthermal plasma synthesis of nanopowdes from organometallic precursors [20]. Methane pyrolysis yielding macromolecular hydrocarbons, changes in the self-ignition limits of combustible mixtures, and other processes initiated by low-temperature plasma have been other objects of investigation. The high rates of these processes are due to the decomposition of the initial compounds in the low-temperature plasma reactor. However, although there have been numerous applied studies in this field [2–21], the mechanism of destruction under these conditions is still not known for certain. It was initially thought that hydrocarbon destruction generally takes place via a free-radical mechanism [21]. However, experimental studies of the destruction kinetics of a large number of hydrocarbons revealed some facts that cannot be explained in terms of the free-radical mechanism alone and indicated the significance of ionic processes [1]. The main flaws of the free-radical mechanism is that it does not account for the concentration dependence of the destruction efficiency, the extraordinarily high destruction efficiency at low concentrations, the marked difference between the concentration dependences of process parameters for different molecules, and the existence of a correlation between the destruction kinetics and the ionization energies of the decomposing substance and dioxygen [1]. At the same time, these observations can readily be explained under the assumption that ions are involved in the process [1].

The main purpose of this work is to study ethane destruction in corona discharge by experiments and simulation. Ethane was selected for this study for the reason that it is the simplest hydrocarbon having the same kinetic characteristics as most hydrocarbons. (It was found that, in this respect, methane is an exception from the alkane homologous series [1].)

Before this study, it was demonstrated by calculations and experimentally that ethane destruction in corona discharge occurs via the same mechanism as the destruction of most hydrocarbons. These calculations were based on a comparison between the ionization potentials of ethane and dioxygen. This correlation was established earlier based on extensive studies of the destruction of hydrocarbons and other molecules in corona discharge [1]. Ethane is the second simplest hydrocarbon after methane. It is, therefore, possible to construct a reliable model for elementary reactions in ethane oxidation and to compare the

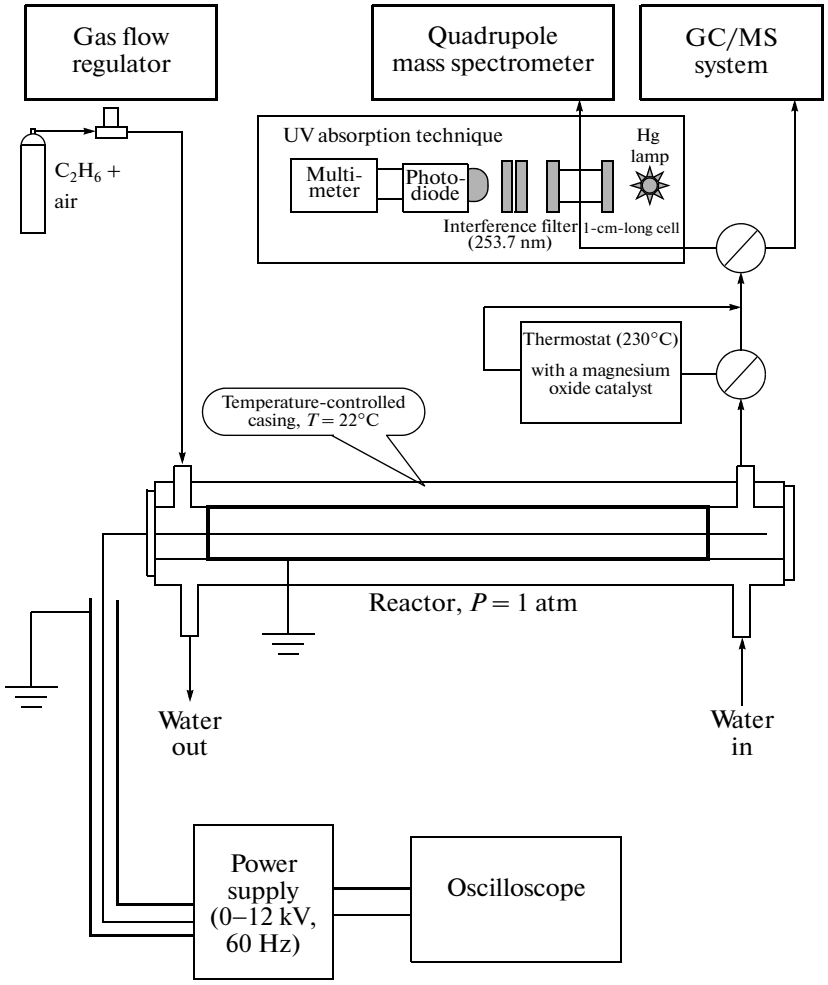

Fig. 1. Experimental setup.

results of calculations for this model with experimental data.

EXPERIMENTAL

The experimental setup used in this study is shown in Fig. 1. A cylindrical ac corona discharge reactor with a dielectric barrier was coupled to a quadrupole mass spectrometer and a GC/MS system. The reactor was a Pyrex tube (80 cm in length and 4 mm in inner diameter) with a Ni–Cr wire inside. The wire was secured at the tube axis and served as the high-voltage electrode. The second (earthed) electrode, made of aluminum foil, clung to outer surface of the tube. Corona discharge was initiated by a high ac voltage (up to 20 kV, 60 Hz) applied to the axial electrode. This produced a uniform discharge throughout the reactor length. The reactant (C_2H_6) and its destruction products were monitored on-line using a Finnigan 4021 quadrupole mass spectrometer and an HP 5973 GC/MS system fitted with a Valco 6-port valve with a 0.25-ml sample loop. The destruction efficiency was studied as a function of absorbed energy density, residence time, and the velocity of the gas flowing through the reactor. The reactor temperature was maintained at 22°C using a water jacket.

The active discharge power (energy consumed by the reactor per unit time) was determined by measuring the voltage and current. The output voltage of the high-voltage transformer was measured using a two-resistor voltage divider. The discharge current was determined from the voltage drop across a resistor placed in series with the earthed output of the high-voltage transformer. The voltage and current were measured with a 54501 HP digitizing oscilloscope. For determining the mean actual power consumed in the reactor, the power data were integrated over a period of time and averaged. The parasitic loss in the high-voltage transformer was determined after the disconnection of the high-voltage cable from the reactor. The measured power loss was subtracted from the active power measured while the reactor was operated. The active power dissipated in the reactor (0–8 W) was

controlled by varying the input voltage of the transformer.

The mass spectra of the reaction mixture were recorded on a quadrupole mass spectrometer at various discharge powers. To avoid ozone destruction, the ion source was maintained at a low temperature of 40°C. The main destruct6ion products (CO_2, CO, and H_2O) were not quantified because of the large errors arising from the strong H_2O background peak and the overlap between the CO and N_2 peaks. The main focus of this study was on the qualitative and quantitative analysis of ethane decomposition intermediates.

The intermediates were identified and quantified by GC/MS using two capillary columns, namely, HP-5MS (30 m × 0.25 mm) and Chrompack Al_2O_3/KCl PLOT (50 m × 0.25 mm). The GC/MS system was calibrated against standard gas mixtures (with air as the diluent gas) prepared in special-purpose 2-l cylinders (Kontess) with a Mininert valve. The mixtures were prepared by syringing prescribed amounts of liquid compounds into a calibrated volume through the valve followed by their evaporation. The calibration compounds were nitromethane, acetaldehyde, propanal, acetic acid, and formic acid (Aldrich), as well as methyl nitrate and ethyl nitrate synthesized [22, 23] and purified by ourselves. The sensitivity coefficients for all compounds were determined relative to propanal as the standard.

In the GC/MS analyses for C_2H_6 and N_2O, we used a Chrompack PLOT column packed with alumina. This column ensured separation of C_1–C_5 hydrocarbons. The GC/MS system was calibrated against commercial gas mixtures of ethane with air and of nitrous oxide (1034 ppm) with nitrogen (Matheson Tri-Gas) and against a multicomponent mixture consisting of 1.00% CO, 1.00% CO_2, 1.00% H_2, 1.01% CH_4, 1.01% O_2, and nitrogen (Scott Specialty Gases). Performing this calibration, we ascertained that the sensitivity of the instrument to each component is stable within 1% over 24 h.

To prevent the failure of the chromatographic columns, the mixture to be analyzed by GC/MS was passed through a reactor heated to 230°C or through a manganese oxide (Aldrich) trap at room temperature in order to remove the ozone formed in the discharge. Manganese oxide is known to be an effective ozone decomposition catalyst even at room temperature [24]. Ozone destruction in the gas mixture sampled at the reactor outlet might change the composition of the sample. In fact, it was demonstrated experimentally that the effect of ozone destruction on the ethane concentration is fairly insignificant (10%). The extent of ozone destruction as a function of the absorbed energy density was measured using a quadrupole mass spectrometer. In these measurements, ozone was not removed from the mixture leaving the reactor.

The ozone concentration at the reactor outlet was determined simultaneously by two independent methods, namely, UV absorption and quadrupole mass spectrometry. The UV absorption method allowed the absolute ozone concentration to be determined reliably at $\lambda = 253.7$ nm using a 1-cm-long cell. The absorption cross section of ozone at this wavelength is 1.15×10^{-17} cm^2 [25]. A small portion of the stream leaving the cell was directed to the ion source of the quadrupole mass spectrometer. The mass spectrometer was thus calibrated for ozone. At ion source temperatures above 140°C, the ozone concentration measured by mass spectrometry was lower than the concentration measured by UV absorption. This was due to ozone decomposition in the ion source. For this reason, the ion source temperature in our measurements was maintained at 40°C.

Certified ethane–air gas mixtures with ethane concentrations of 12, 109, 1033, and 10000 ppm (Matheson) were used in ethane destruction experiments.

Propanal C_2H_5CHO (97%), ethanol (97%), methanol (99.93%), and acetic acid (99.5%) were purchased from Aldrich and were used as received. For calibrating the GC/MS system with an HP-5 column, we prepared a mixture consisting of C_2H_5CHO (1940 ppm), nitromethane CH_3ONO_2 (2190 ppm), acetic acid (2450 ppm), and helium balance and a mixture consisting of C_2H_5CHO (150 ppm), CH_3ONO_2 (20 ppm), C_2H_5OH (190 ppm), and helium balance.

MODEL OF FREE-RADICAL REACTIONS

The experimental data were compared with the results of simulation using the ChemKin II program [26] and a model of free-radical reactions. This model consists of a number of electron impact–induced molecule dissociation steps and 809 subsequent reactions involving 85 atoms, free radicals, and excited species. It is based on Konnov's ethane oxidation mechanism [27]. Konnov's initial mechanism, developed for high-temperature hydrocarbon oxidation, consists of over 1200 elementary reactions, including reactions involving nitrogen-containing compounds [27]. We modified this mechanism by leaving only the reactions involving C_1 and C_2 compounds, C_2H_5CHO, and C_2H_5CO. The reactions involving HOCN, HNCO, C_2N_2, CNN, HCNN, HCNH, N_2H_2, N_2H_3, and N_2H_4 were excluded. The mechanism was augmented by adding 85 reactions that are significant at the low temperatures used in this work. Data for these reactions were taken from the NIST database. Four reactions of the CH_3O and C_2H_5O radicals with NO and NO_2 [22, 23] were also added.

The initiation of the reactions was described as the formation of oxygen and nitrogen atoms, mainly in excited states, via the dissociation of the major components of the reaction mixture under the action of an

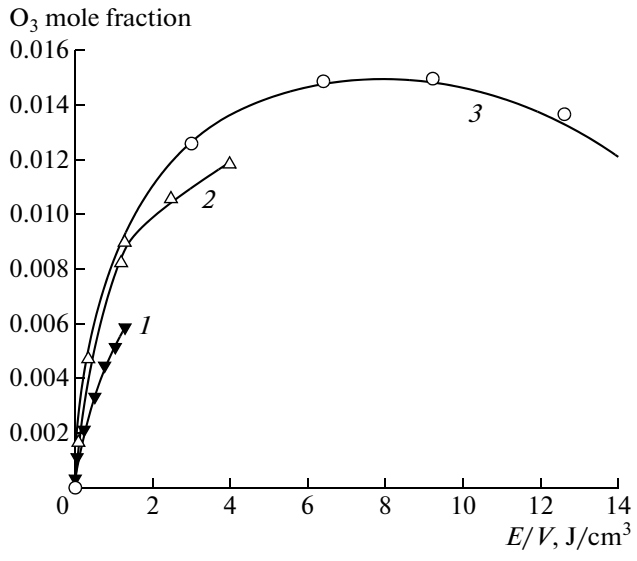

Fig. 2. Experimental data on ozone formation in air under the action of corona discharge at flow rates of (*1*) 6, (*2*) 1.2, and (*3*) 0.5 cm^3/s.

electron impact. The initiation process includes the electron-impact dissociation of dioxygen [28–30]:

$$O_2 + e^- \rightarrow O + O(^1D) + e^-, \quad \text{(I)}$$

$$O_2 + e^- \rightarrow O + O + e^-, \quad \text{(II)}$$

$$N_2 + e^- \rightarrow N + N(^2D) + e^-. \quad \text{(III)}$$

In addition, we included the electron impact–induced dissociation reactions of ozone (which can accumulate up to high concentrations) and water (since water is a final product, its concentration must be proportional to the amount of ethane decomposed; moreover, water is a source of reactive hydroxyl radicals):

$$O_3 + e^- \rightarrow O_2 + O(^1D) + e^-, \quad \text{(IV)}$$

$$H_2O + e^- \rightarrow H + OH + e^-. \quad \text{(V)}$$

The ozone and N_2O formation rates measured in the absence of ethane at various flow rates in the reactor and various discharge powers were used to determine the rates of the initiation reactions yielding oxygen atoms.

RESULTS AND DISCUSSION

Ozone Formation in Corona Discharge: Experiments and Simulation

Experimental data on ozone formation in artificial air in the absence of ethane are presented in Fig. 2. The ozone formation rate is determined by dissociation processes (I)–(IV) caused by an electron impact. The rate constants of these processes can be calculated from the active discharge power consumed in the rector and the corresponding radiation yields (G). The radiation yield G is defined as the number of elementary events per 100 eV of absorbed energy and is widely used in radiation chemistry [31].

In order to make use of the known relative efficiencies of electron impact–induced processes, we took the following simplified approach. We assumed that the radiation yield of the ith process in a mixture in which the mole fraction of the ith component is x_i ($G_{i,xi}$) is proportional to this mole fraction:

$$G_{i,xi} = G_{i,xi0}x_i/x_{i0}. \quad (1)$$

Here, x_{i0} and $G_{i,xi0}$ are the mole fraction of the ith component and the radiation yield of the corresponding process at this mole faction, respectively, known from the literature, calculated, or obtained experimentally.

The first-order rate constant of electron impact–induced dissociation, k_i, is expressed in terms of the radiation yield ($G_{i,xi0}$, number of elementary events/100 eV), the known concentration of the ith component (x_{i0}), and specific absorbed power (P_v, J cm^{-3} s^{-1}):

$$k_i = (1/389.2)P_vG_{i,xi0}/x_{i0}. \quad (2)$$

It is assumed here that G is measured (or calculated) for a gas mixture with the same component concentrations as in the mixture for which this formula is used. The absorbed energy density P_v is derived from the reactor volume (V, cm^3) and the total power dissipated by the reactor (P, W):

$$P_v = P/V. \quad (3)$$

The radiation yields for the dissociation of O_2, O_3, N_2, and H_2O are known from the literature [28–30]. Note that G may depend on the parameters of the reactor and, accordingly, vary from one reactor design to another. The most significant reactor parameter is the decrease in the electric field strength in the streamers, which is close to the breakdown field strength [30, 32]. In turn, the latter is determined by the diameter of the axial electrode: the smaller the diameter, the higher the breakdown field strength [33]. The effect of field weakening on the radiation yields was taken into account as follows. The relative radiation yields for the field strength specified in the streamers were taken from the literature [28–30] (G_{lit}). The field strength in the streamers was taken to be equal to the breakdown field strength [30, 32]. The G values obtained in this way were multiplied by the coefficient Z_R, which was determined by comparing the experimental and calculated dependences of the ozone concentration on the energy absorbed by the reactor:

$$G_i = G_{i(lit)}Z_R. \quad (4)$$

The literature G data used in this work are listed in Table 1. The measured ozone concentrations and the concentrations calculated using the accepted mechanism are plotted in Fig. 3. The Z_R value determined in this experiment is 0.31.

The calculated maximum ozone yield is 22 molecule/100 eV at a reduced field strength of 110–130 T [28], while the observed ozone yield is only 13.9 mol-

Table 1. Radiation yield for the most significant processes induced by an electron impact

Reaction no.	Reaction	G_i	Z_R	$G_{i(\text{lit})}$ (literature data)
1	$O_2 \longrightarrow O + O(^1D)$	2.48	0.31	8 [30]
2	$O_2 \longrightarrow O + O$	0.62	0.31	2 [30]
3	$O_3 \longrightarrow O_2 + O(^1D)$	15.5	–	54 [28, 29]*
4	$N_2 \longrightarrow N + N(^2D)$	0.17	0.31	0.217 [30]
5	$H_2O \longrightarrow O + OH$	2.24	0.31	14 [29]

* Calculated from the ratio of the radiation yield for reaction (3) to the sum of the reaction yields for reactions (1) and (2).

ecule/100 eV [28], implying that the radiation yields in processes 1 and 2 (Table 1) are 6.95 molecule/100 eV each. At low ozone concentrations in our experiments, the total ozone yield from reactions (1) and (2) was 3.1 (Table 1). Therefore, the parameters of the reactor are not optimal for ozone generation. This is due to the fact that the weakening of the electric field in the reactor (reduced break down field strength of 350 ± 50 T) is much greater than is required for optimal ozone generation (approximately 135 T [28]).

The radiation yields as a function of the mean electron energy (which depends on the electric field strength) were taken from [32]. The G values calculated for the reduced field of $E/N = (350 \pm 50)$ T are listed in Table 1. The ratio of the radiation yield of ozone dissociation (reaction (3) in Table 1) to the total yield of dioxygen dissociation (reactions (1) and (2) in Table 1) for experimental conditions similar to those used in this work is 5 ± 3, according to experiments, calculations, and the literature [28, 29]. Based on this value, the radiation yield of ozone dissociation is $G_3 =$ 15.5 (at an O_3 mole fraction of 0.21 and a pressure of 1 bar) (Table 1).

The formation rate constants of active components calculated using modified G values for particular experimental conditions ($P = 3.6$ W, $V = 10.0$ cm^3) are given in Table 2. According to the above model, a constant oxygen atom concentration is established under these conditions, which is approximately 0.1 ppm. The establishment of this constant concentration takes about 14 μs (characteristic time of the ozone formation reaction $O + O_2 + M \rightarrow O_3 + M$). Calculations demonstrate that ozone buildup to 3% raises the equilibrium concentration of oxygen atoms by <10%, irrespective of whether ethane is present.

The concentration of oxygen atoms is mainly determined by the following three reactions: oxygen atom formation (reaction (1) in Table 2) and ozone formation reactions involving dioxygen (reactions (7) and (8) in Table 3).

Calculations demonstrate that the ozone yield depends only on the absorbed energy density (E/V) and is independent of the flow rate. This situation is observed experimentally only at low absorbed energy densities (or low ozone concentrations). This is clear from Fig. 3, in which the initial portions of all curves have the same slope. However, the model does not provide a correct description for the dependence of the ozone concentration on the flow rate at high absorbed energy densities. The initial slope of the curves in Fig. 3 was used in the calibration of the radiation yields for reactions (1)–(5) from Table 1. The model qualitatively accounts for the fact that, at high absorbed energy densities (>50 J/cm^3), the ozone concentration stops growing and the nitrogen oxide yield increases, as is shown in Fig. 4. This is in agreement with experimental data of other authors [20].

Destruction Kinetics of C_2H_6 in Air in Corona Discharge as a Function of the Absorbed Energy Density

Figure 5 illustrates the destruction kinetics of 1% ethane in air in corona discharge. The ratio of the ethane concentration at the reactor outlet to the ethane concentration at the inlet, $[C_2H_6]_{out}/[C_2H_6]_{in}$, is plotted here versus the absorbed energy density for different flow rates. The corresponding calculated

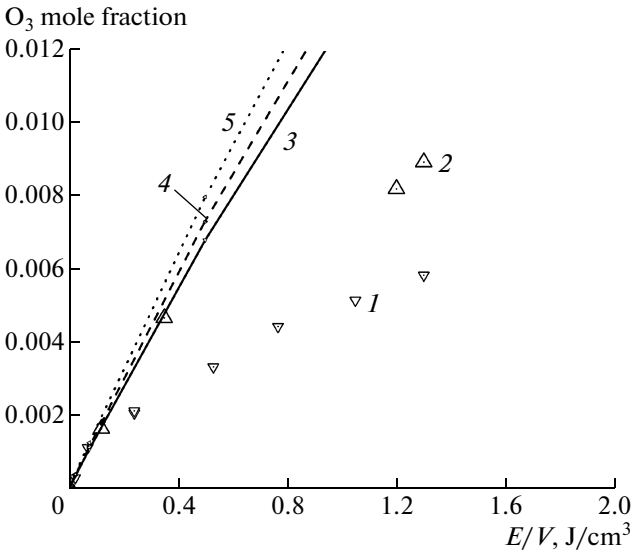

Fig. 3. Results of the simulation of ozone formation in air under the action of corona discharge: (*1*, *2*) experimental data and (*3*–*5*) calculated data for flow rates of (*1*, *5*) 6, (*2*, *4*) 1.2, and (*3*) 0.5 cm^3/s.

Table 2. Reactions of O_2, O_3, N_2, and H_2O under the action of an electron impact and their kinetic parameters

Reaction no.	Reaction*	A, s^{-1}	b	E, cal/mol
1	$O_2 \longrightarrow O + O(^1D)$	1.09×10^{-2}	0	0
2	$O_2 \longrightarrow O + O$	2.72×10^{-3}	0	0
3	$O_3 \longrightarrow O_2 + O(^1D)$	6.80×10^{-2}	0	0
4	$N_2 \longrightarrow N + N(^2D)$	9.52×10^{-4}	0	0
5	$H_2O \longrightarrow O + OH$	1.90×10^{-2}	0	0

* The rate constants were calculated as $k = AT^b\exp(-E/RT)$ using data from Table 1 and Eqs. (1)–(4). Experimental conditions: $P = 3.6$ W, reactor volume of 10 cm^3, flow rate of 1.2 cm^3/s, residence time of 8.35 s, absorbed energy density of 3.0 J/cm^3.

data are also presented here. The observed destruction kinetics (ethane concentration as a function of the absorbed energy density) is pseudoexponential and can be fitted to the following equation:

$$[C_2H_6]_{out}/[C_2H_6]_{in} = A\exp(-E_v/E_{v0}), \qquad (5)$$

where $A = 0.4$, E_v is determined by the ratio of the power to the flow rate (J/cm^3), and $E_{v0} = 9.5$ J/cm^3.

The destruction parameter E_{v0} [1] is derived from the slope of the initial portion of the curve at power/flow rate ratios of 0.004 and 1 J/cm^3. The calculated extent of ethane destruction is several times lower than is observed experimentally. This discrepancy increases as the ethane concentration decreases.

The lower limit of ethane combustion in air is 3%. At an ethane concentration of 1%, the mixture did not ignite in spite of the continuous energy input and, accordingly, the presence of active species. As the same time, the observed extent of destruction was higher than the extent of destruction calculated for the radical chain kinetic mechanism.

Products and Their Yield in Ethane Destruction in Air in Corona Discharge

The ultimate destruction products (water and carbon dioxide) were detected by mass spectrometry. No quantification of these compounds was performed. Formaldehyde, acetaldehyde, methanol, ethanol, formic and acetic acids, nitromethane, methyl nitrate, and ethyl nitrate were identified among the intermediate compounds. Ethanol, nitromethane, methyl nitrate, ethyl nitrate, and acetic acid were determined quantitatively. A broad chromatographic peak was observed at low ethane concentrations. After the identification of the observed mass spectrum using the NIST mass spectral library, this peak was assigned to 3,3'-oxydi-(1,2-propanediol) tetranitrate ($C_6H_{10}N_4O_{13}$).

Figure 6 plots the relative yields of products per decomposed ethane molecule for the 1% C_2H_6 + air mixture and shows the results of simulation. For this initial ethane concentration, the model qualitatively describes the formation of all of the observed components; however, it provides no quantitative fit to experimental data. The quantitative discrepancy between the calculated and observed data becomes still greater as the ethane concentration is decreased. The model leads to higher yields of these products (which are due to free-radical reactions) as compared to the experimental data.

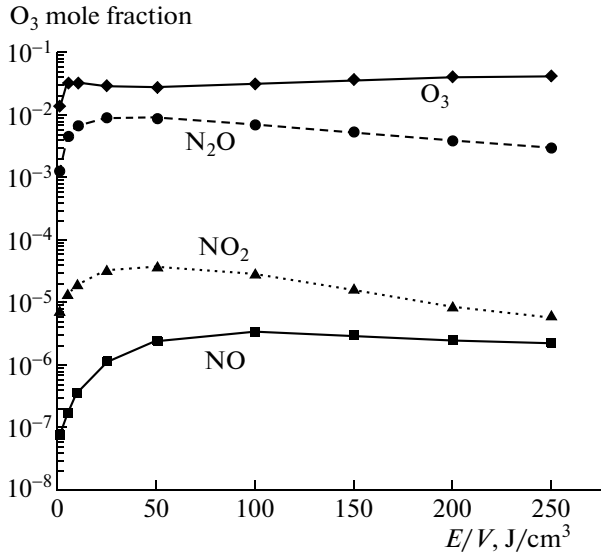

Fig. 4. Results of the simulation of ozone and nitrogen oxide formation in air under the action of corona discharge. The residence time is 100 s.

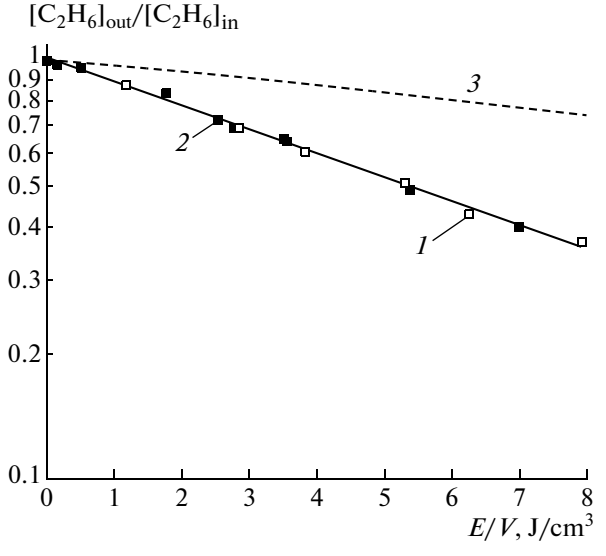

Fig. 5. Extent of C_2H_6 destruction in corona discharge as a function of the energy density: (*1*, *2*) experimental data and (*3*) calculated data at flow rates of (*1*, *3*) 1.2 and (*2*) 2.5 cm^3/s.

Table 3. Elementary reactions added to Konnov's mechanism [27] from the NIST 98 database [34] and from [22, 23]

Reaction no.	Reaction*	A*	b	E, cal/mol
6	$O_3 + O \longrightarrow O_2 + O_2$	4.82×10^{12}	0	4094
7	$O + O_2 + O_2 \longrightarrow O_3 + O_2$	1.84×10^{21}	−2.8	0
8	$O + O_2 + N_2 \longrightarrow O_3 + N_2$	1.72×10^{21}	−2.8	0
9	$O + O + M \longrightarrow O_2 + M$	1.00×10^{17}	−1	0
10	$O + NO + O_2 \longrightarrow NO_2 + O_2$	8.86×10^{20}	−1.8	0
11	$O + NO + N_2 \longrightarrow NO_2 + N_2$	3.30×10^{20}	−1.6	0
12	$O + N_2 + M \longrightarrow N_2O + M$	1.82×10^{10}	0	0
13	$O + NO_2 = NO + O_2$	3.91×10^{12}	0	−238
14	$O + N_2O_5 \longrightarrow O_2 + NO_2 + NO_2$	1.81×10^{8}	0	0
15	$N + N + M \longrightarrow N_2 + M$	4.53×10^{15}	0	0
16	$N + O + M \longrightarrow NO + M$	1.98×10^{15}	0	−0.3
17	$N + NO_2 \longrightarrow N_2 + O_2$	4.20×10^{11}	0	0
18	$N + NO_2 \longrightarrow N_2 + O + O$	5.50×10^{11}	0	0
19	$N + NO_2 \longrightarrow N_2O + O$	3.49×10^{12}	0	−0.4
20	$N + NO_2 = NO + NO$	1.00×10^{12}	0	0
21	$N + N_3 \longrightarrow N_2 + N_2$	3.60×10^{13}	0	0
22	$N + N_2O_5 \longrightarrow NO + NO_2 + NO_2$	6.00×10^{8}	0	0
23	$N + O_3 \longrightarrow NO + O_2$	1.21×10^{8}	0	0
24	$NO + O_3 \longrightarrow NO_2 + O_2$	1.08×10^{12}	0	2722
25	$NO_2 + O_3 \longrightarrow NO_3 + O_2$	7.23×10^{10}	0	4869
26	$NO_2 + O_3 \longrightarrow O_2 + O_2 + NO$	6.00×10^{5}	0	0
27	$NO + O_2 + M = NO_3 + M$	2.00×10^{7}	0	417
28	$NO + N_3 \longrightarrow N_2O + N_2$	7.20×10^{11}	0	0
29	$NO_2 + NO_3 = N_2O_5$	3.86×10^{11}	0.2	0
30	$O(1D) + O_2 \longrightarrow O + O_2$	1.93×10^{13}	0	−133
31	$O(1D) + N_2 \longrightarrow O + N_2$	1.08×10^{13}	0	−213
32	$O(1D) + O_3 \longrightarrow O_2 + O_2$	1.45×10^{14}	0	0
33	$O(1D) + N_2O \longrightarrow NO + NO$	4.34×10^{13}	0	0
34	$O(1D) + N_2O \longrightarrow N_2 + O_2$	2.65×10^{13}	0	0
35	$O(1D) + N_2 + M \longrightarrow N_2O + M$	4.04×10^{7}	0	0
36	$O(1D) + NO \longrightarrow O_2 + N$	5.10×10^{13}	0	0
37	$O(1D) + NO_2 \longrightarrow O_2 + NO$	1.80×10^{14}	0	0
38	$N(2D) + O_2 \longrightarrow N + O_2$	3.60×10^{12}	0	0
39	$N(2D) + O_2 \longrightarrow NO + O$	3.60×10^{12}	0	0
40	$N(2D) + NO \longrightarrow N_2 + O$	6.00×10^{13}	0	0
41	$N(2D) + N_2O \longrightarrow NO + N_2$	1.20×10^{14}	0	0
42	$NO + N \longrightarrow N_2 + O$	1.26×10^{13}	0	−200
43	$N + O_2 = NO + O$	9.00×10^{9}	1	6500
44	$NO_2 + NO_2 = NO + NO + O_2$	3.95×10^{12}	0	27590
45	$NO_2 + NO_2 = NO_3 + NO$	1.13×10^{4}	2.6	22720
46	$NO_2 + O\ (+ M) \longrightarrow NO_3\ (+ M)$	1.33×10^{13}	0	0
47	$NO_3 + O \longrightarrow NO_2 + O_2$	1.02×10^{13}	0	0
48	$NO_3 + NO_3 = NO_2 + NO_2 + O_2$	5.12×10^{11}	0	4870
49	$N_2O_4\ (+ M) = NO_2 + NO_2\ (+ M)$	4.05×10^{18}	−1.1	12840

Table 3. (Contd.)

Reaction no.	Reaction*	A*	b	E, cal/mol
50	$N_2O_4 + O \longrightarrow N_2O_3 + O_2$	1.21×10^{12}	0	0
51	$NO_2 + NO\ (+ M) = N_2O_3\ (+ M)$	1.60×10^{9}	1.4	0
52	$N_2O_3 + O \longrightarrow NO_2 + NO_2$	2.71×10^{11}	0	0
53	$O_3 + H \longrightarrow OH + O_2$	6.03×10^{13}	0	729
54	$O_3 + OH \longrightarrow HO_2 + O_2$	1.15×10^{12}	0	1987
55	$O_3 + HO_2 \longrightarrow OH + O_2 + O_2$	8.43×10^{9}	0	1192
56	$O_3 + HONO \longrightarrow HNO_3 + O_2$	3.01×10^{5}	0	0
57	$O_3 + CO \longrightarrow CO_2 + O_2$	2.40×10^{-1}	0	0
58	$O_3 + HCO \longrightarrow H + CO_2 + O_2$	5.00×10^{11}	0	0
59	$O_3 + CH_3 \longrightarrow CH_3O + O_2$	1.57×10^{12}	0	0
60	$O_3 + CH_3O \longrightarrow CH_3O_2 + O_2$	1.21×10^{9}	0	0
61	$O_3 + C_2H_5 \longrightarrow C_2H_5O + O_2$	2.00×10^{10}	0	0
62	$O_3 + C_2H_4 \longrightarrow CH_3HCO + O_2$	5.50×10^{9}	0	0
63	$O_3 + CH_3HCO \longrightarrow CH_3CO + OH + O_2$	3.60×10^{3}	0	0
64	$O_3 + C_2H_4O \longrightarrow CH_3CO + OH + O_2$	3.60×10^{3}	0	0
65	$O_3 + C_2H_6 \longrightarrow C_2H_5OH + O_2$	2.37×10^{11}	0	14300
66	$C_2H_5O_2 + C_2H_5O_2 \longrightarrow CH_3HCO + C_2H_5OH + O_2$	1.39×10^{10}	0	0
67	$C_2H_5O_2 + C_2H_5O_2 \longrightarrow C_2H_5O + C_2H_5O + O_2$	2.46×10^{10}	0	0
68**	$C_2H_5O + NO_2 \longrightarrow C_2H_5ONO_2$	1.70×10^{10}	0	0
69	$C_2H_5O + NO_3 \longrightarrow C_2H_5O_2 + NO_2$	2.00×10^{12}	0	0
70	$C_2H_5O_2 + NO_3 \longrightarrow C_2H_5O + NO_2 + O_2$	2.00×10^{12}	0	0
71	$C_2H_5O_2 + NO \longrightarrow C_2H_5O + NO_2$	5.20×10^{12}	0	0
72	$C_2H_5O_2 + NO \longrightarrow C_2H_5ONO_2$	7.20×10^{10}	0	0
73**	$CH_3O + NO_2 = CH_3ONO_2$	1.20×10^{10}	0	0
74**	$CH_3O_2 + NO = CH_3O + NO_2$	2.50×10^{9}	0	−0.4
75**	$CH_3O_2 + NO = CH_3ONO_2$	7.50×10^{7}	0	−0.4
76	$CH_3O_2 + O = CH_3O + O_2$	3.60×10^{13}	0	0
77	$NO_3 + CH_4 = HNO_3 + CH_3$	6.00×10^{5}	0	0
78	$NO_3 + CH_2O = HNO_3 + HCO$	3.50×10^{8}	0	0
79	$NO_3 + CH_3HCO = HNO_3 + CH_3CO$	8.40×10^{11}	0	3696
80	$NO_3 + C_2H_2 = HNO_3 + C_2H$	6.00×10^{7}	0	0
81	$NO_3 + C_2H_6 = HNO_3 + C_2H_5$	6.00×10^{6}	0	0
82	$NO_3 + C_2H_5 \longrightarrow C_2H_5ONO_2$	2.40×10^{13}	0	0
83	$NO_3 + CH_3 \longrightarrow CH_3ONO_2$	2.10×10^{13}	0	0
84	$NO_3 + CH_3O = CH_2O + HNO_3$	8.00×10^{11}	0	0
85	$NO_3 + CH_3O = CH_3O_2 + NO_2$	1.20×10^{12}	0	0

* $k = AT^b\exp(-E/RT)$. The units of A are s^{-1} for the first-order reactions and $cm^3\ mol^{-1}\ s^{-1}$ for the second-order reactions.
** Reactions were taken from [22, 23].

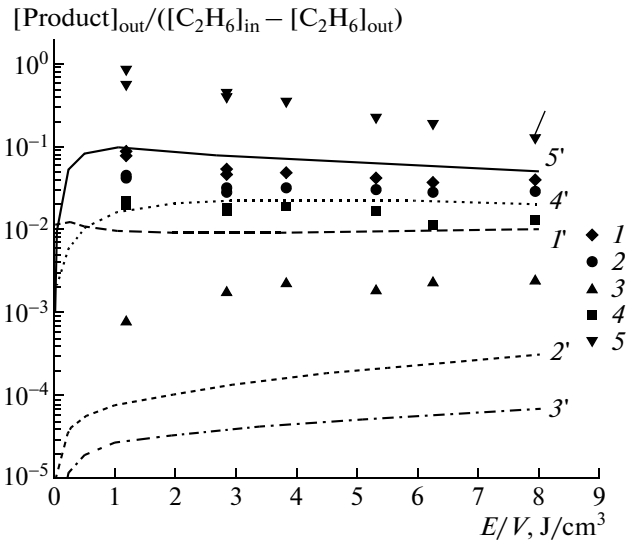

Fig. 6. (*1*–*5*) Experimental and (*1'*–*5'*) calculated relative concentrations of (*1*, *1'*) $CC_2H_5ONO_2$ (*2*, *2'*) CH_3ONO_2, (*3*, *3'*) CH_3NO_2, (*4*, *4'*) C_2H_5OH, and (*5*, *5'*) $CH_3C(O)OH$ for the destruction of 1% C_2H_6 in air under the action of corona discharge.

The observed set of nitrogen-containing products is in agreement with the following simplified mechanism. The main C-containing products of the primary stages of destruction (no matter what the nature of these processes) are ethyl and methyl radicals (C_2H_5 and CH_3). They can result from the abstraction of an H atom from the ethane molecule involved in a free-radical, ion–molecule, or dissociative ion–electron neutralization reaction or directly from electron impact–induced dissociation.

The model considered here, which ignores ion–molecule reactions, cannot adequately account for the observed absolute ethane destruction efficiency. Nevertheless, it is clear that the product composition at the reactor outlet is largely determined by secondary free-radical reactions. Some of the identified destruction products can result from the reactions given below.

At moderate temperatures, an important role in oxygen-containing mixtures is played by peroxy radicals. As a consequence, methoxyl and ethoxyl radicals [34] form via the reactions

$$C_2H_5 + O_2(+M) = C_2H_5O_2(+M), \quad (86)$$

$$CH_3 + O_2(+M) = CH_3O_2(+M), \quad (87)$$

$$CH_3 + O_3 \rightarrow CH_3O + O_2, \quad (88)$$

$$C_2H_5 + O_3 \rightarrow C_2H_5O + O_2, \quad (89)$$

$$CH_3O_2 + O = CH_3O + O_2, \quad (90)$$

$$CH_3O_2 + CH_3O_2 \rightarrow CH_3O + CH_3O + O_2, \quad (91)$$

and via reactions (66), (70), (71), and (74) (Table 3).

The subsequent reactions of the methoxyl, ethoxyl, methyl peroxy, and ethyl peroxy radicals yield nitrates [22, 23, 34] via reactions (68), (72), (73), and (75) (Table 3). These products can also result directly from the interaction of the ethyl and methyl radicals with NO_3 [34] (reactions (82) and (83) in Table 3).

Other observed reaction products, such as CH_3NO, C_2H_5OH, and $CH_3C(O)OH$, are also predicted by the free-radical mechanism.

Along with the products resulting from secondary free-radical reactions, one more compound was observed, which showed itself as a comparatively broad chromatographic peak. Identification of its mass spectrum using the NIST mass spectral library demonstrated that this compound is 3,3'-oxydi-(1,2-propanediol) tetranitrate ($C_6H_{10}N_4O_{13}$). The amount of this product is relatively small at high ethane concentrations. For 1% ethane in air, the peak area for this product is only 3% of the total area of all peaks. As the ethane concentration is decreased, the relative concentration of this compound increases.

CONCLUSIONS

Ethane destruction in air in corona discharge with a dielectric barrier was studied in detail by experiments and simulation. The model qualitatively describes the destruction efficiency (to within the order of magnitude) at an initial ethane concentration of 1%. The quantitative analysis of the reaction products indicates unambiguously that the free-radical mechanism cannot account for the experimental observations. The results of this work provide a procedure for investigating and modeling the destruction of various substances in low-temperature plasma with the aim of removing detrimental impurities, obtaining new components, and initiating the ignition of combustible mixtures.

ACKNOWLEDGMENTS

This work was supported by grants from NATO Linkage Grant (DISRM.LG961353) and US Army Research Office (DAAG55-98-0068).

REFERENCES

1. Krasnoperov, L.N., Krishtopa, L.G., and Bozzelli, J.W., *J. Adv. Oxid. Technol.*, 1997, vol. 1, no. 3, p. 1.
2. Yamamoto, T., Ramanathan, K., Lawless, Ph.A., Ensor, D.S., Newsome, J.R., Plaks, N., and Ramsey, G.H., *IEEE Trans. Ind. Appl.*, 1992, vol. 28, no. 3, p. 528.
3. Storch, D.G. and Kushner, M.J., *J. Appl. Phys.*, 1993, vol. 73, no. 1, p. 51.
4. Chang, M.B. and Lee, C.C., *Environ. Sci. Technol.*, 1995, vol. 29, no. 3, p. 181.
5. Sano, N.Z., Nagamoto, T., Tamon, H., Suzuki, T., and Okazaki, M., *Ind. Eng. Chem. Res.*, 1997, vol. 36, no. 3, p. 3783.
6. Fitzimmons, C., Ismail, F., Whitehead, J.C., and Wilman, J.J., *J. Phys. Chem. A*, 2000, vol. 104, no. 6, p. 6032.

7. Clothiaux, E.J., Koropchak, J.A., and Moore, R.R., *Plasma Chem. Plasma Process.*, 1984, no. 4, p. 15.
8. Fraser, M.E., Eaton, H.J., and Sheinson, R.S., *Environ. Sci. Technol.*, 1985, vol. 19, no. 2, p. 946.
9. Korobeinichev, O.P., Chernov, A.A., Sokolov, V.V., and Krasnoperov, L.N., *Int. J. Chem. Kinet.*, 2002, vol. 34, no. 5, p. 331.
10. Ohkubo, T., Kanazavwa, S., Nomoto, Y., Chang, J.-Sh., and Adachi, T., *IEEE Trans. Ind. Appl.*, 1994, vol. 30, no. 4, p. 856.
11. Chang, M.B., Kushner, M.J., and Rood, M.J., *Environ. Sci. Technol.*, 1992, vol. 26, no. 1, p. 777.
12. Penetrane, M.B., Hsiao, M.C., Merrit, B.T., and Vogtlin, G.E., *IEEE Trans. Plasma Sci.*, 1995, vol. 23, no. 4, p. 679.
13. Urashima, K., Chang, J.Sh., and Ito, T., *IEEE Trans. Ind. Appl.*, 1997, vol. 33, no. 4, p. 879.
14. Masuda, S., *J. Appl. Chem.*, 1988, vol. 60, no. 5, p. 727.
15. Sun, W., Pashaie, B., Dhali, S.K., and Honea, F.I., *J. Appl. Phys.*, 1996, vol. 79, no. 7, p. 3438.
16. Onda, K., Kasuga, Y., Kato, K., Fujiwara, M., and Tanimoto, M., *Energy Convers. Manage.*, 1997, vol. 38, p. 1377.
17. Chang, M.B., Balbach, J.H., Rood, M.J., and Kushner, M.J., *J. Appl. Phys.*, 1991, vol. 69, no. 8, p. 4409.
18. Harano, A., Sadakata, M., and Sato, M., *J. Chem. Eng. Jpn.*, 1991, vol. 24, no. 1, p. 100.
19. Spiess, F.J., Chen, H., Brock, S.L., Suib, S.L., Hayashi, Y., and Matsumoto, H., *J. Phys. Chem. A*, 2000, vol. 104, no. 12, p. 11111.
20. Remnev, G.E. and Pushkarev, A.I., *IEEJ Trans. Fundam. Mater.*, 2004, vol. 124, no. 6, p. 483.
21. Evans, D., Rosocha, L.A., Anderson, G.K., Coogan, J.J., and Kushner, M.J., *J. Appl. Phys.*, 1993, vol. 74, no. 9, p. 5378.
22. Scholtens, K.W., Messerer, B.M., Cappa, C.D., and Elrod, M.J., *J. Phys. Chem. A*, 1999, vol. 103, no. 4, p. 4378.
23. Ranschaert, D.L., Schneider, N.J., and Elrod, M.J., *J. Phys. Chem. A*, 2000, vol. 104, no. 5, p. 5758.
24. Li, W., Gibbs, G.V., and Oyama, S.T., *J. Phys. Chem. A*, 1998, vol. 120, no. 10, p. 9041.
25. DeMore, W.B., Sander, S.P., Golden, D.M., Hampson, R.F., Kurylo, M.J., Howard, C.J., Ravishankara, A.R., Kolb, C.E., and Molina, M.J., *Chemical Kinetics and Photochemical Data for Use in Stratospheric Modeling*, 1992, no. 10, p. 106.
26. Kee, R.J., Rupley, F.M., and Miller, J.A., *Chemkin-II: A FORTRAN Chemical Kinetics Package for the Analysis of Gas Phase Chemical Kinetics*, Sandia Nat. Lab. Rep. SAND89-8009B UC-76, 1992.
27. Konnov, A.A., *28th Symp. (Int.) on Combustion*, Edinburgh, 2000, p. 317.
28. Eliasson, H.M. and Kogelschatz, U., *J. Phys. B: At. Mol. Phys.*, 1986, vol. 19, no. 2, p. 1241.
29. Peyrous, R., Pignolet, P., and Held, B., *J. Phys. D: Appl. Phys.*, 1989, vol. 22, no. 3, p. 1658.
30. Penetrane, M.B., Hsiao, M.C., Bardsley, J.N., Merrit, B.T., Vogtlin, G.E., Wallman, P.H., Kuthi, A., Burkhart, C.P., and Bayless, J.R., *Phys. Lett. A*, 1995, vol. 209, no. 1, p. 69.
31. Hughes, G., *Radiation Chemistry*, Oxford: Clarendon, 1973.
32. Penetrane, M.B., Hsiao, M.C., Merrit, B.T., Vogtlin, G.E., Wallman, P.H., Neiger, M., Wolf, O., Hammer, T., and Broer, S., *Appl. Phys. Lett.*, 1996, vol. 68, no. 26, p. 3719.
33. Lowke, J.J. and Morrow, R., *Pure Appl. Chem.*, 1994, vol. 66, no. 6, p. 1287.
34. Mallard, W.G., Westley, F., Herron, J.T., Hampson, R.F., and Frizzell, D., *NIST Chemical Kinetics Database—NIST Standard Reference Database 17-2Q98*, Gaithersburg, Md.: NIST, 1998.